Journal of The Electrochemical Society, 2022 **169** 046509

Optical Modulation and Phase Distribution in $LiCoO_2$ upon Li-Ion De/Intercalation

Sanaz Banifarsi,[=] Yug Joshi,[=,z] Robert Lawitzki, Gábor Csiszár, and Guido Schmitz

Chair of Materials Physics, Institute of Materials Science, University of Stuttgart, 70569 Stuttgart, Germany

Modulation of reflectance resulting from the change in optical constants in Li_xCoO_2 during lithium de/intercalation is studied and quantified by in-operando and ex situ optical spectroscopy. To this aim, the $LiCoO_2$ (LCO) thin films are sputter deposited using radio-frequency ion-beam sputtering. The films are structurally characterized by X-ray diffraction and transmission electron microscopy. The reversible electrochemical and electrochromic performance is determined by in-operando optical reflectance. Ex-situ reflectance, at particular charge states, is used to determine the optical constants by modeling the optical spectrum using the Clausius-Mossotti relation. The model reveals a dominant resonant wavelength at 646 nm for the fully intercalated state of LCO. For the delithiated state or $Li_{0.5}CoO_2$, a much broader and significantly larger absorption peak is obtained by the model description. This significantly broad and intense absorption peak can be associated with the conducting nature of the films upon lithium removal. Furthermore, the observed complex refractive index (CRI), evolving with the lithium content, is justified by the prior reported density of states calculations. With the CRI, the corresponding variation of the real and imaginary part of the dielectric function reveals that the intercalation of lithium and the consequent phase propagation follows a layer-like reaction.
 [DOI: 10.1149/1945-7111/ac63f6]

Manuscript submitted January 18, 2022; revised manuscript received March 15, 2022. Published April 14, 2022.

Lithium cobalt oxide (LCO) has been in commercial use for over three decades in rechargeable lithium-ion batteries.[1] The high-temperature phase of LCO has a layered hexagonal structure where CoO_6 octahedra form alternate layers between which Li can de/intercalate reversibly.[2,3] Goodenough et al.[4] introduced $LiCoO_2$ as a battery electrode material because of the ability to reversibly insert/remove Li. The oxidation state of Co increases because of the Li removal. The half-cell compensation reaction is given by Eq. 1.

$$Li(Co^{3+})O_2 \xrightarrow{0 \leqslant z \leqslant 0.5} Li_{1-z}(Co^{3+}_{1-z}Co^{4+}_{z})O_2 + Li^+_z + ze^- \quad [1]$$

There are two phase-transformations known to occur during the above-mentioned Li deintercalation (i.e. $1 \geqslant x \geqslant 0.5$ in Li_xCoO_2). First, a first-order phase transition from a hexagonal and insulating $Li_{1\geqslant x\geqslant 0.975}CoO_2$ ($R\bar{3}m$, a = 2.82 Å, c = 14.08 Å, in hexagonal setting, labelled hexagonal type I)[5,6] into a hexagonal metallic $Li_{0.75\geqslant x\geqslant 0.5}CoO_2$ ($R\bar{3}m$, a = 2.81 Å, c = 14.37 Å, in hexagonal setting, hexagonal type II).[5,6] Second, a transition from the hexagonal to a monoclinic symmetry (C2/m, a = 4.88 Å, b = 2.82 Å, c = 5.06 Å and β = 107.93°) initiated at $Li_{0.5}CoO_2$.[7,8] These order transitions in the crystal structure of LCO during Li intercalation also cause a change in electronic structure.[9,10] The variation of electronic properties of the material upon lithiation must also influence the optical properties. These properties, in principle, can be used to probe the phase propagation using a dense, geometrically-defined thin film of LCO.[11–15] But one may also envision a technical function in optical switching, e.g. by coating a LCO layer onto a silicon or silicon nitride waveguide for producing signal modulation by insertion/removal of lithium).[16] For this, the dependence of the optical constants on the Li content is required. Other applications include the use as an electrochromic material (i.e. materials showing a change of color upon ion insertion via an electrochemical reaction) in smart windows and mirrors. WO_3 remains the state of the art for such application using either hydrogen[17] or lithium implantation[18,19] to achieve a change in color. Other materials include alloys of Magnesium,[20,21] Nickel oxide,[22] Yttrium Hydride,[23] Vanadium oxide[24] etc (see the recent review on electrochromism).[25]

In this study, firstly an observable change in optical reflectivity in LCO upon de/lithiation is established using in-operando measurements. Subsequently, the change in complex refractive index (CRI) of the material upon dis-/charging is evaluated by modeling ex situ measurements applying the Clausius-Mossotti relation.[12,26–28] Such quantitative evaluation enables the determination of the different optical transitions governing the CRI of the material. Consequently, the bandgap for the lithiated sample is also revealed. Finally, the microstructural information, together with dielectric constants for the phase separating material, yields the geometrical distribution of individual phases.[12,29,30]

Experimental

Sample preparation.—Thin films were grown in a custom-made deposition chamber hosting a radio frequency ion beam source (Rau & Roth 4 cm ∅) operating at 13.56 Mhz.[31–33] The base pressure of the deposition chamber (ultra-high vacuum) was 1×10^{-7} mbar. A platinum disk and a cold-pressed sintered powder of $LiCoO_2$ (LCO, from EXM 1058, Südchemie) were used as targets for the sputtering process.[34] A 180 nm thick platinum film was deposited on an oxidized Si wafer with ⟨001⟩ orientation using only argon gas. For the deposition of $LiCoO_2$, oxygen was added as a reactant gas such that the Ar:O ratio was 7:3.[34] A 205 nm thick layer of LCO was sputtered in this study. The deposited multilayers were annealed at 750 °C for 1 h at ambient atmosphere, to make them electrochemically active. In earlier work, we demonstrated that the EELS spectra of the so produced films and of the LCO target material are very similar confirming correct chemical composition.[34] A further point to note, the produced LCO films remain stable until 850 °C,[35] hence the used annealing temperature will not significantly affect the stoichiometry of the films.

Electrochemical characterization.—The electrochemical characterization was executed by the software *EC-Lab* controlling a potentiostat (Bio-Logic VSP-300 with six independent channels). The cyclic voltammetry (CV) measurement was performed using a three-electrode setup as shown in Fig. 1a. Two lithium foils were used as counter and reference electrodes, hence all the potentials in this paper are with respect to lithium. LCO is the working electrode in the electrochemical cell. The electrolyte used in this study was 1 M $LiClO_4$ dissolved in a 1:1 ratio of ethylene carbonate and dimethyl carbonate (by mass). The assembly of the cell was executed in an argon-filled glove box. In cyclic voltammetry, the potential is varied from 3.6 V to 4.2 V vs Li/Li (the upper boundary is limited to 4.2 V to avoid irreversible phase transformations[34]).

[=]These authors contributed equally to this work
[z]E-mail: yug.joshi@mp.imw.uni-stuttgart.de

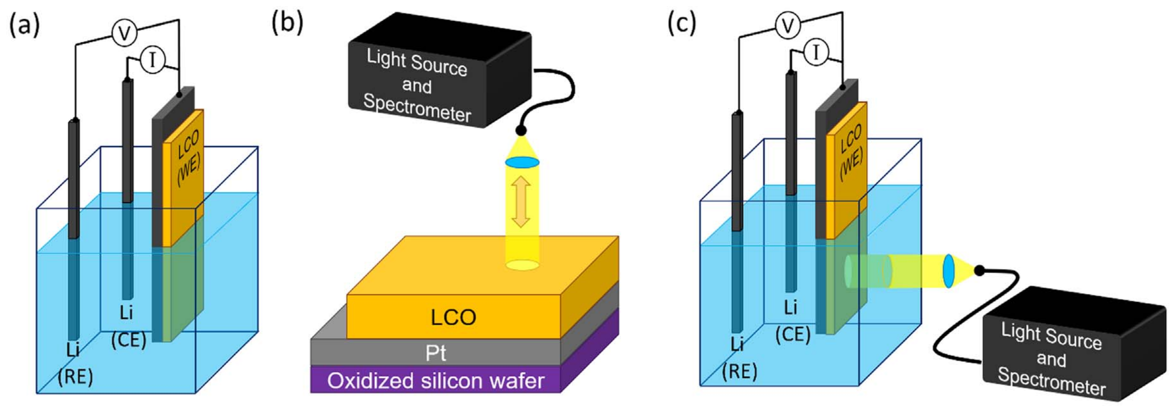

Figure 1. Schematics of: (a) a three-electrode cell used for electrochemical characterization and to achieve quasi-equilibrium charge states; (b) an ex situ optical reflectance measurement; (c) in-operando optical reflectance measurements during electrochemical dis-/charging.

For the quantification of the CRI, quasi-equilibrium charge states are measured optically using an ex situ approach. To obtain a defined charge state (for ex situ optical reflectance spectroscopy), a sequence of galvanostatic (chronopotentiometry) followed by the potentiostatic (chronoamperometry) technique is applied to the electrochemical cell. The potentiostatic step is maintained till the current saturates down to a value less than 0.2 μA·cm^{-2}. The sample is subsequently cleaned with dimethyl carbonate.

Structural characterization.—The crystallinity of the thin films, on a macro scale, is verified by X-ray diffraction (XRD) using Co-Kα radiation generated at 40 kV and 35 mA. The XRD spectra are collected on a Bruker D8 diffractometer in a Bragg-Brentano geometry. Also, the microstructure has been characterized by transmission electron microscopy (TEM) using a Philips CM-200 FEG TEM operated at 200 kV. The electron transparent TEM specimens are prepared by the standard FIB lift-out technique[36] with a FEI SCIOS dual beam instrument.

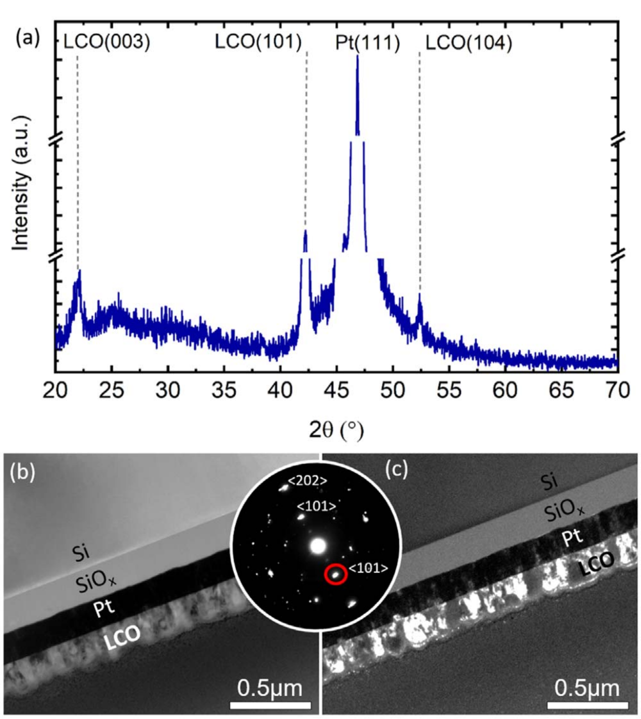

Figure 2. (a) XRD pattern of thin-film (i.e. LCO on Pt) after annealing at 750 °C. (b) bright-field TEM image and (c) dark-field TEM image highlighting grains with their [101] orientation parallel to the growth direction during ion beam deposition (Chosen reflection marked in the SAED pattern in the inset figure).

Optical characterization.—The electrochromic response or the change in the optical behavior of the LCO thin-film was investigated by reflectance spectroscopy via in-operando and ex situ approaches.

In-operando reflectance.—Reflectance spectra were recorded during electrochemical operation of the battery i.e. during cyclic voltammetry. The electrochemical control was executed with the potentiostat *Interface 1000* (Gamry Instruments). The optical spectra were recorded by an *Exemplar* (BW-Tek) spectrometer. The electrochemical cell is made up of a cuvette with flat quartz glass windows, it consists of a LCO thin-film deposited on top of Pt acting as a working electrode, and two lithium strips acting as a reference and a counter electrode, see Fig. 1c,[12,28] A parallel beam of light from a tungsten halogen lamp is illuminating the sample normally (perpendicular to the surface). The resulting reflected light is collected and diverted to the spectrometer. The ion conduction between the electrodes is made possible by using the same electrolyte i.e., 1 M $LiClO_4$ in 1:1 ethylene carbonate and dimethyl carbonate.

Ex-situ reflectance.—A specific charge state is obtained by the sequence of galvanostatic and potentiostatic sequence, as described above. The optical spectra at these charge states are obtained using the same *Exemplar* spectrometer. The only difference is that the sample is in ambient air during the optical measurement (whereas in the in-operando case, the electrolyte was in contact with the surface of LCO). Various charge states of Li_xCoO_2 (x = 0.5, 0.62, 0.75, 0.88, 0.99, and 1) are probed in these measurements.

Results and Discussion

Structural characterization.—Figure 2a shows the XRD pattern of the annealed LCO film on a platinum current collector. The strongest peak at 46.8° corresponds to Pt (111) which has the highest scattering cross-section of all studied elements. In addition to the Pt peak, three significant peaks can be observed in the spectrum that corresponds to the (003), (101), and (104) planes of LCO (R $\bar{3}$ m). It should be noted that the relative intensity of the peaks does not match to the powder diffraction data of LCO.[37] According to these standard data, the (003)- peak should reveal the highest intensity, while the obtained diffractogram clearly shows a higher intensity of the (101)- peak. This indicates a preferential orientation of the (101)-planes in a fiber texture along the growth direction, which is typical for sputter-deposited thin films.[28] In confirmation, the microstructure of the thin films has been characterized by TEM. The morphology of the thin-film is shown in the cross-section image in Fig. 2b. LCO grows in a columnar microstructure. The circular inset of the figure

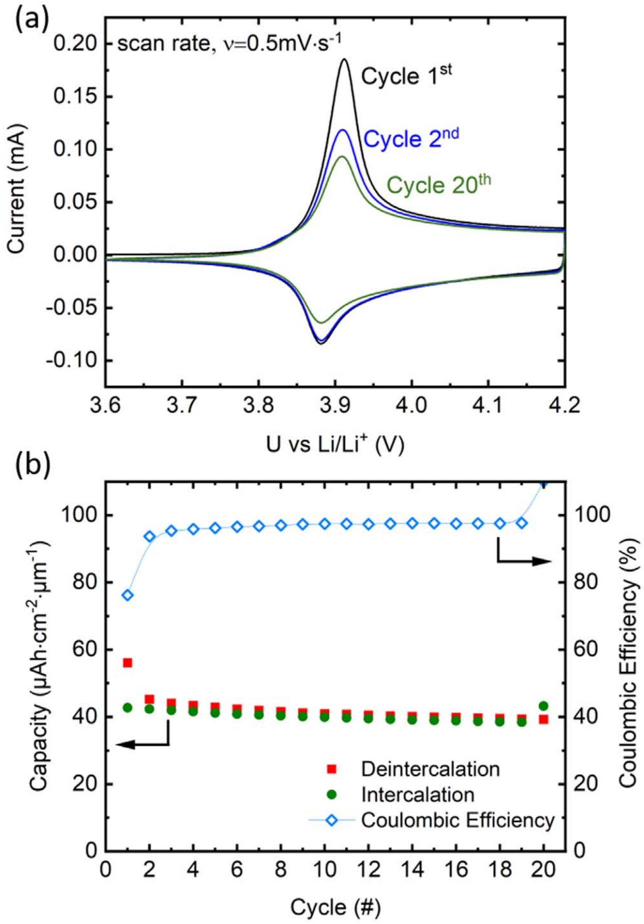

Figure 3. (a) 1st, 2nd and 20th cycle during cyclic voltammetry of the LCO thin film at a scan rate of 0.5 mV·s^{-1}; (b) calculated capacity during 20 cycles.

shows the selected area electron diffraction (SAED) pattern of the LCO thin-film. As can be seen, spots corresponding to ⟨101⟩ and ⟨202⟩ lattice planes, having more brightness, when aligned normal to the substrate, meaning the corresponding lattice planes are lying parallel to the substrate. A dark-field TEM obtained by using one of these intense (101)- reflections (highlighted by a red circle in the inset figure), is shown in Fig. 2c. The predominantly bright areas confirm a preferential texture along the (101)- direction. This result is in good agreement with the XRD. A film thickness of around 205 nm can be determined from the TEM bright-field image.

Electrochemical characterization.—Figure 3a shows cyclic voltammograms (1st, 2nd and 20th cycle), of the LCO thin film annealed at 750 °C in air, with a scan rate of 0.5 mV·s^{-1}. The CV cycles were limited between a voltage window of 3.6 V to 4.2 V to avoid irreversible chemical decomposition of LCO. The kinetics of lithium insertion in the LCO may depend on the texture of the sample as the migration of the lithium is expected to be anisotropic in the layered atomic arrangement.[38] Figure 3a indicates that for the first cycle, the main intercalation and deintercalation peaks appear at 3.88 V and 3.91 V, respectively. According to previous studies, the first phase transition in delithiation occurs at 3.92 V, which corresponds to a two-phase reaction that causes a discontinuous change in lattice constant but no change in the crystal symmetry (i.e. one hexagonal phase transforms into another one).[5,8,39,40] In the second cycle, the area of the redox peaks has decreased indicating a capacity fading, which is presumably due to irreversible side reactions at high voltages of 4.2 V. Gu et al.[41] have reported the redox peaks maximum decreases due to the degradation of the crystal or interface structure of LCO. Afterward, however, between the 2nd and the 20th cycle, the drop in the peak current or the capacity (cf Fig. 3) becomes less significant. Figure 3b shows the capacity evolution with cycling. Only in the first cycle, a relatively large loss in the capacity is observed, which is also evident from the low coulombic efficiency or charge reversibility (light blue diamonds) in the first two cycles. Later, the capacity stabilizes at 40 μAh·cm^{-2}·μm^{-1}. Hence, it can be stated that the prepared thin-films show reversible de/intercalation sufficient to study optical effects.

Optical characterization.— *In-operando.*—After establishing a reversible electrochemical behavior, the optical performance of the thin-film electrodes is probed using in-operando reflectance spectroscopy. The results of these measurements are summarized in Fig. 4. Figure 4a shows a CV measurement during Li deintercalation of the 29th cycle (last cycle) with a scan rate of 0.5 mv·s^{-1}. The last in-operando cycle was chosen because the redox reaction stabilizes after long-term cycling. The colored arrows in the CV curve mark the selected states of charge for which the reflectance spectra are shown in Fig. 4b. It should be pointed out that the surface of the Pt layer, deposited underneath the LCO film, reflects all of the incident light and hence, acts as a perfect mirror in the optical spectroscopy. The surface of the LCO layer in contact with the electrolyte represents another optical active interface. Multiple reflections at the interfaces provoke interference, which causes fringes (maxima and minima) in the optical spectrum (hence the spectrum appears wavy with maxima at ca. 500 nm and 1000 nm). When a single wavelength of 950 nm is considered, as in Figs. 4c and 4d, the reflectance decreases during Li- deintercalation from about 35% to 25%, and vice versa during intercalation. The reduction in the reflectance (or increase in absorbance) is most probably due to the transition from insulating (or semiconductive) to metallic behavior due to Li- deintercalation. Furthermore, the reversibility of the change of reflectance in different cycles is exhibited in Fig. 4c. From the tested cycles 21st to cycle 29th, the reflectance is highly reversible during cycling. The quantitative relation between reflectance and state of charge is given in Fig. 4d. It is seen that a continuous decrease in reflectance appears with deintercalation in the full cycled range i.e., between $1 \geqslant x \geqslant 0.5$ in Li_xCoO_2.

Ex-situ.—Ex-situ reflectance spectra avoid the possible disturbing impact of the liquid electrolyte. They were obtained at different states of charge, established after 30 cycles, as shown by hollow circles in Fig. 5b. The Li content has been calculated by integrating the current from the galvanostatic step and subsequent potentiostatic step. It is assumed here that a voltage of 4.2 V corresponds to a composition of $x = 0.5$ in Li_xCoO_2.[40] The ex situ reflectance spectra upon delithiation show a similar trend as the in-operando measurement (compare Figs. 4b and 5b). A point to note is the overall lower reflectance in the in-operando measurement, probably due to the additional absorption of light by the electrolyte or the different nature of the top interface (LCO/air versus LCO/electrolyte) (discussed later).

For fully lithiated Li_xCoO_2 or $x = 1$, the first reflectance maximum is located at 543 nm, and further subsequent fringes are distinguishable. By releasing Li from the Li_xCoO_2 structure, this maximum shifts to a lower wavelength of ca. 533 nm, and almost disappears after further removal of Li i.e., when $x < 0.62$. The peak shifting upon Li removal is probably due to a change in the real part of the CRI (complex refractive index) being responsible for the modulation of the wavelength within the material (see section on Optical constants). The averaged decrease of reflectance and diminishing of the fringes indicates that also the imaginary part of the CRI, responsible for absorption of light (see section on Optical constants) varies with the Li content.

A detailed point to note is the very significant reflectance change from $x = 1$ to $x = 0.99$ in Li_xCoO_2 indicating a phase transition. This change is not observed in the in-operando measurements, probably due to the dynamic nature of the method. However, it becomes very

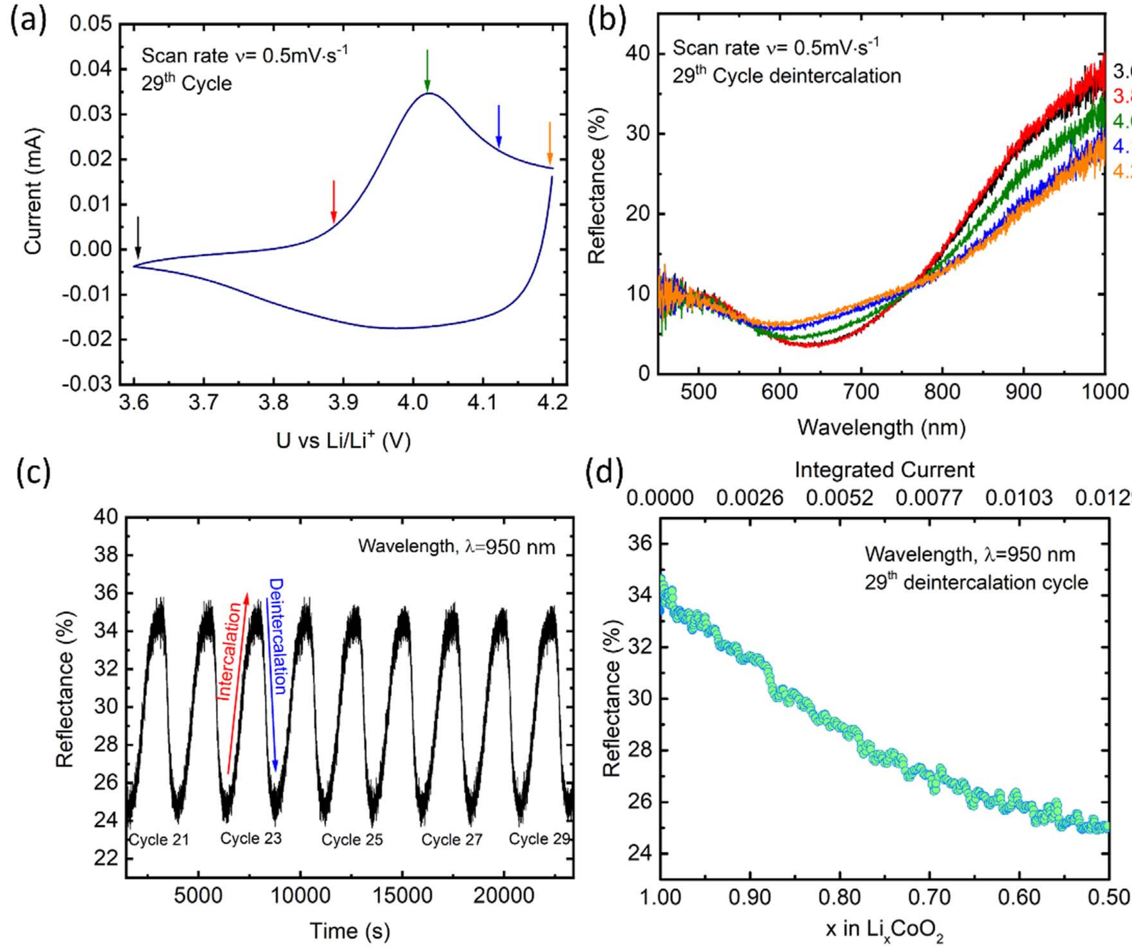

Figure 4. (a) cyclic voltammetry curve of cycle 29; (b) in situ optical reflectance spectra corresponding to selected voltages indicated in the CV curve; (c) change in reflectance with time at constant wavelength, $\lambda = 950$ nm; (d) change of the reflectance with Li content during deintercalation.

clear in the ex situ measurements. According to a study by Ménétrier,[42] the solid solution with a hexagonal type $_{\mathrm{I}}$ crystal structure exists for lithium contents of $1 \geqslant x \geqslant 0.94$. On the other hand, they reported that this hexagonal type $_{\mathrm{I}}$ structure has insulating properties, whereas the hexagonal type II behaves like a metal. Interestingly, their data showed a change of conductivity as soon as the Li content dropped below $x = 0.98$. Therefore, both statements (i.e., the solubility range or the fact that conductivity increase is associated with the formation hexagonal type II) cannot be true simultaneously. This discrepancy probably arises from the structural similarity of the hexagonal type I and II phases which hinders early phase identification in XRD spectra. In our data, from Fig. 5a, it can be seen that even the smallest deintercalation of Li initiates the phase transformation, marked by the start of the plateau in the galvanostatic measurements i.e. the solubility limit of the hexagonal type $_{\mathrm{I}}$ phase must be close to $x = 0.99$ which is also close to the phase boundary reported by Zhang and White ($x = 0.975$).[6] The remaining slight difference could be due to minor chemical deviation in the Li content arising from the sputter-deposition process. For the hexagonal type II phase, the solubility range in Li_xCoO_2 has been reported to be $0.75 \geqslant x \geqslant 0.5$.[5,6,42] The high Li boundary of this range is confirmed in the present study, by the optical reflectivity (negligible change in reflectance beyond $x = 0.75$, see Fig. 5b).

Optical constants.—In the following, we extract the complex refractive index and its dependence on the Li content from the experimental data. The CRI (given by $n_\alpha^*(\lambda)$ for medium α) has a real part and an imaginary part, coupled together in the form of Eq. 2.

$$n_\alpha^*(\lambda) = n_\alpha(\lambda) - i \cdot k_\alpha(\lambda) \tag{2}$$

where the real part of the CRI ($n_\alpha(\lambda)$) is defined as the ratio of the phase velocity of an electromagnetic (EM) wave when traveling in vacuum to that in medium α. The imaginary part of CRI ($k_\alpha(\lambda)$) describes the absorption of light by the medium α.[43] The absorption can be written in terms of the Beer-Lamberts law as.[44,45]

$$A_\alpha = A_{0,\alpha} \cdot e^{-\frac{2\pi}{\lambda} \cdot k_\alpha \cdot L}, \tag{3}$$

where $A_{0,\alpha}$ and A_α are the initial and final amplitudes of the EM wave, L is the optical path length and λ is the wavelength.

Using the above definitions, a model description of the experiment is developed. The ambient atmosphere, the LCO thin-film, and the platinum current collector are assigned as the first, second, and third medium, through which light has traversed, respectively. The bottom platinum layer reflects all the light. A pure Pt thin film (100 nm) was used as a reference (the measured reflected intensity is stated with respect to the reflectivity of pure Pt, i.e., it is assumed Pt acts as a perfect mirror). Based on the summation of all reflected amplitudes of light, the total reflectance at normal incidence is given by Eq. 4 as.[12,46]

$$R(d, \lambda)\% = \left| \left(\frac{r_{12} + r_{23} \cdot e^{-i\frac{2\pi}{\lambda} n_2^* \cdot 2d}}{1 + r_{12} r_{23} \cdot e^{-i\frac{2\pi}{\lambda} n_2^* \cdot 2d}} \right) / r_{13} \right|^2 \times 100 \tag{4}$$

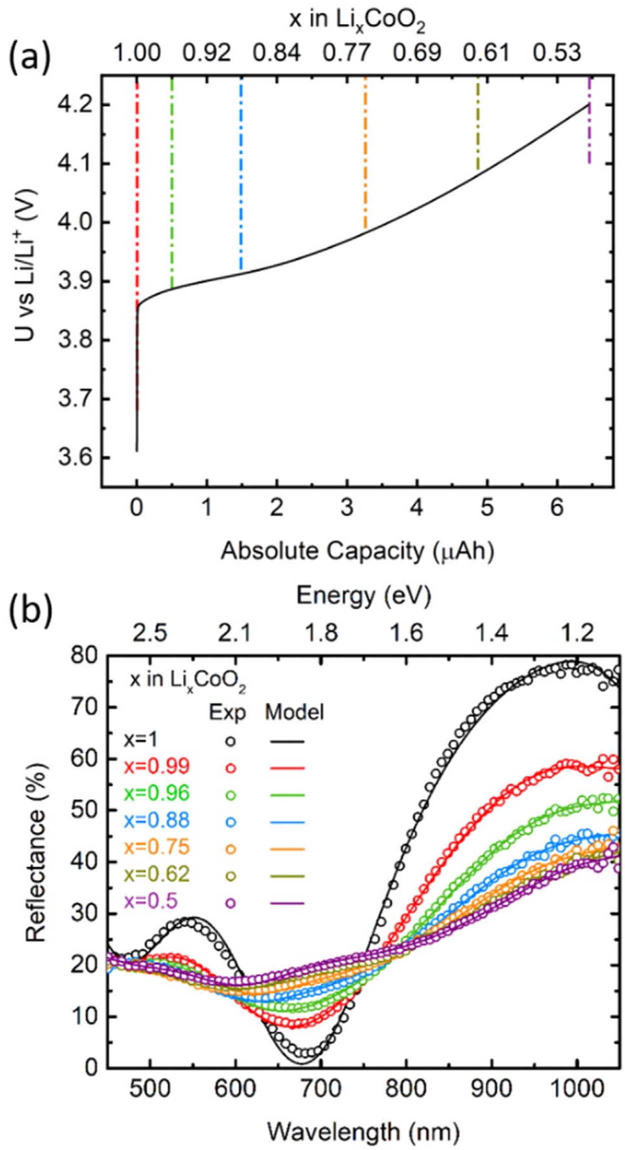

Figure 5 (a) CP measurement of LCO in which dashed lines show the selected Li contents for ex situ spectroscopy; (b) Optical reflectance spectra of the ex situ measurements for different Li contents. Hollow circles present the experimental results, solid lined the result of the model description.

where r_{12}, r_{23}, r_{13} are the reflection coefficients between air-LCO, LCO-platinum, and reference air-Pt, respectively; d is the thickness of the film, n_2^* is the CRI of LCO. For normal incidence, the Fresnel's reflection coefficient between media α and β is given by

$$r_{\alpha\beta} = \frac{n_\beta^* - n_\alpha^*}{n_\beta^* + n_\alpha^*} \quad [5]$$

where n_α^* is the CRI of medium α. For determining r_{23} and r_{13}, the CRI of the platinum is obtained from Werner et al.[47] The refractive index of ambient air is assumed to be 1. Now, combining Eqs. 4 and 5, the only remaining unknown is the CRI of LCO. Therefore, the model description is completed by defining the missing refractive index of LCO. For this, a modified Lorentz dispersion relation is used. While the classical Lorentz dispersion model describes the interaction of incident EM waves with the electron cloud, it does not consider interatomic interactions (or more correctly, the polarization of the electron cloud due to the neighboring atoms). Therefore, a modified Lorentz dispersion equation, known as the Clausius-Mossotti relation is applied, which is given by Eq. 6.[26,27]

$$\frac{(n_\alpha^*)^2 - 1}{(n_\alpha^*)^2 + 2} = \frac{N q_e^2}{3\, \epsilon_0\, \mathrm{m_e}} \sum_j \left(\frac{f_j}{\omega_{0j}^2 - \omega^2 + i \cdot \omega \gamma_j} \right) \quad [6]$$

where N is the number of electrons per volume, q_e elementary charge, ϵ_0 free space permittivity, $\mathrm{m_e}$ the mass of the electron, f_j the strength of the j^{th} oscillator, ω_{0j} the resonance frequency of the j^{th} oscillator, γ_j the respective damping factor, and ω $(=2\pi/\lambda)$ the frequency of the incident EM wave.

The reported reflectance spectra obtained by the ex situ measurements (Fig. 5b are quantitatively evaluated, using this model description, to understand the interaction of light with LCO and how it evolves upon de/lithiation. Three independent oscillators were used i.e., j varies between 1 and 3 in Eq. 6. The resulting modeled spectra are shown by continuous lines in Fig. 5b. The confidence of fitting (adjusted R^2) even in the worst situation is about 0.9992, observed for the fully intercalated ($x = 1$) LCO. Therefore, from Fig. 5b, the model description is confirmed to be fitting neatly to the experimental data. The parameters of the fitted curves are presented in Table I. Noteworthy, the resonance frequency of the third oscillator is not in the spectral range of the spectrometer. However, it is necessary to allow a reasonable description of the data.

From the fitted data, the extinction coefficients and the refractive indexes are calculated in dependence on the wavelength as shown in Fig. 6. Figures 6a and 6b show the change in the imaginary part and the real part of the CRI, respectively. For a fully intercalated state ($x = 1$ in Li_xCoO_2), a relatively sharp absorption peak is observed at the wavelength around 646 nm (λ_{01}) which corresponds to the first oscillator. Considering the color spectrum in the visible region, the Li_1CoO_2 seems to absorb red light and hence reflects blue and green light. By contrast, there is a much broader and significantly larger absorption peak covering almost the entire visible range (i.e. 450 nm $< \lambda <$ 700 nm) for $x = 0.5$ in Li_xCoO_2. Thus, the color of the delithiated LCO should be blackish. Obviously, these color changes are only qualitative but they match the decrease in the intensity of white light passing through a LCO layer as reported by Berkemeier et al.[15]

The absorption process must be linked to the electronic excitation (in the visible region of light). So, to understand the sharp absorption peak of the completely lithiated LCO, the density of states (DOS) at this charge-state[48] is considered as shown by the black solid line in Fig. 6d. The Fermi level (marked by the dotted vertical line) of Li_1CoO_2 is located within the band-gap, hence marking it as an insulator or a semiconductor. The dominant transition energy or the peak maximum of the extinction coefficient of 646 nm (or 1.9 eV) matches perfectly to the transitional energy between the filled Co-t_{2g} band and the empty Co-$e_{.g.}$ band. Hence, we may assign this absorption peak to the electronic transition across the band-gap. This band-gap value is comparable to other literature values although the theoretical data fluctuate somewhat, i.e., 1.7 eV,[49] 2.1 eV,[49] 2.5 eV[50] and 2.7 eV[51] for HT-LCO. It has to be mentioned that the stoichiometry, composition, and purity of LCO can affect the energy of the band gap from the experimental side.

Now, from Fisg. 6a and 6c, it can be seen that the dominant peak of the extinction coefficient shifts to lower wavelengths or higher energy upon delithiation. This indicates a broadening of the energy gap with the electronic transition. This phenomenon is demonstrated when comparing the theoretical DOS of $Li_{0.99}CoO_2$ and $Li_{0.97}CoO_2$ given by red dashed and green dashed-dotted lines in Fig. 6d, as they were reported in.[48] Upon delithiation, both, the Co-t_{2g} and the Co-$e_{.g.}$ bands shift towards higher energy with respect to the Fermi level (in fact, a decrease of the Fermi level with deintercalation is the more intuitive understanding). However, this shift is more dominant in the case of the Co-$e_{.g.}$ band; thereby, widening the energy gap and increasing the energy of the electronic transition. The general

Table I. Fitting Parameters for three oscillators for different Lithium concentration

x in Li_xCoO_2	Nf_1	$\lambda_{01}(nm)$	$\gamma_1 \times 10^{15}$ $(rad.s^{-1})$	Nf_2	$\lambda_{02}(nm)$	$\gamma_2 \times 10^{15}$ $(rad.s^{-1})$	Nf_3	$\lambda_{03}(nm)$	$\gamma_3 \times 10^{15}$ $(rad.s^{-1})$	Quality of fit, R^2
x = 1	0.45	646 ± 3	0.43	0.36	469.24	1.26	0.01	1079.21	0.17	0.9992
x = 0.999	0.88	605 ± 2	0.52	0.41	458.30	1.55	0.03	1080	0.38	0.9998
x = 0.96	1.27	579 ± 2	0.64	0.36	454.14	1.49	0.03	1080	0.42	0.9997
x = 0.88	1.78	546 ± 2	0.79	0.23	445.63	1.31	0.03	1080	0.44	0.9997
x = 0.75	1.67	542 ± 2	0.82	0.61	483.17	1.02	0.02	1061.22	0.41	0.9996
x = 0.62	1.52	521 ± 2	0.94	1.25	482.24	1.11	0.02	1079.27	0.36	0.9997
x = 0.50	1.50	517 ± 2	0.97	1.50	475.76	1.12	0.01	1075.29	0.30	0.9997

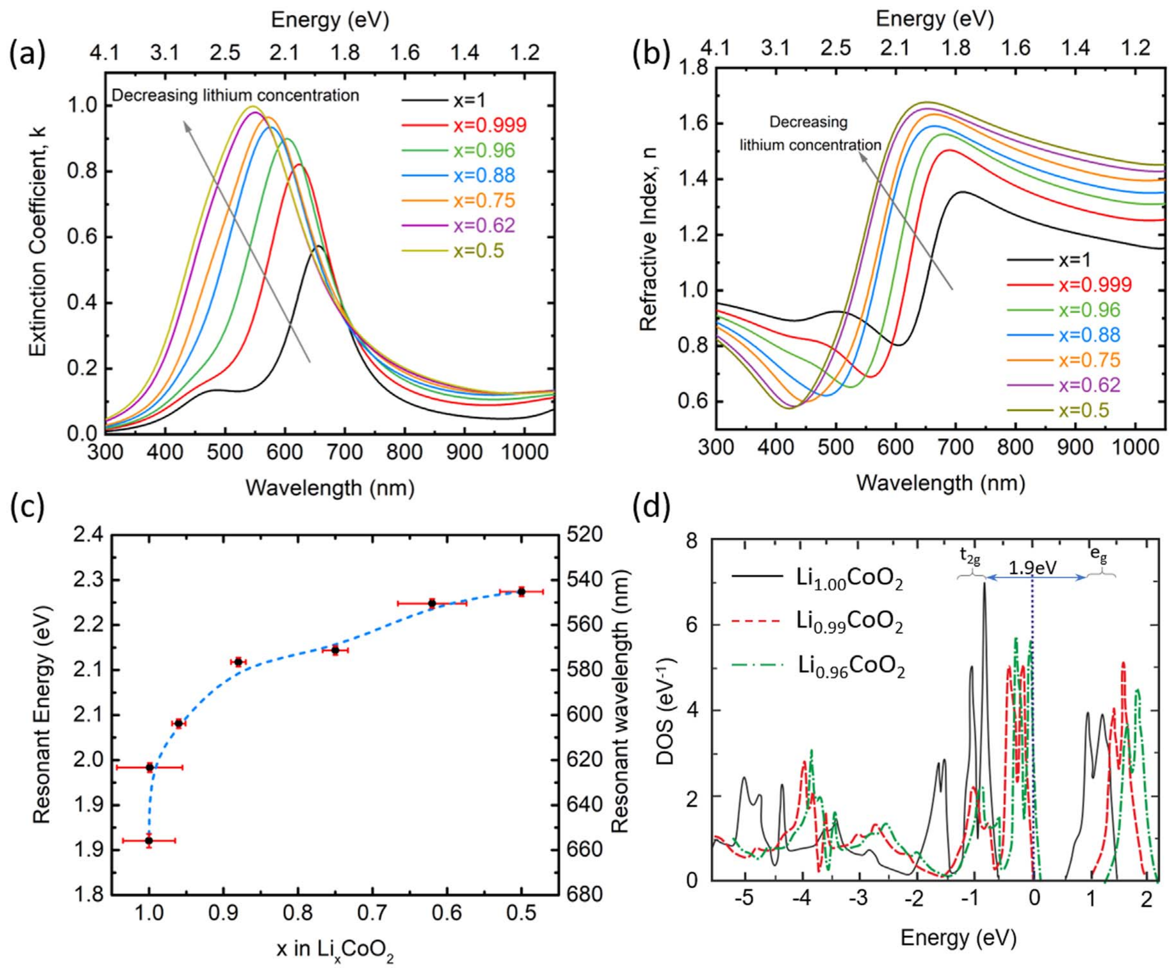

Figure 6. (a) and (b) Imaginary part and real part of the CRI calculated by modeling, respectively; (c) The variation of resonant energy versus Li content in LCO which is interpolated by a B-Spline; (d) Density of states of Li_1CoO_2 (black line), $Li_{0.99}CoO_2$ (red dashed line) and $Li_{0.96}CoO_2$ (green dashed-dotted line), according to.[48]

decrease in the Fermi level with deintercalation is due to the removal of electrons along with the lithium atoms and this phenomenon can be clearly seen for other battery electrodes as well, e.g. $LiMn_2O_4$[28] and $Li_4Ti_5O_{12}$.[12] However, the widening of the transition energy observed in this case is different from the cases of $LiMn_2O_4$ and $Li_4Ti_5O_{12}$. This is probably due to the different electronic transitions, in the case of LCO (from Co-t_{2g} to Co-$e_{.g.}$) whereas in $LiMn_2O_4$ and $Li_4Ti_5O_{12}$ (O-2p to Ti/Mn t_{2g}).

Another detail to note is the immediate shift of the Co-t_{2g} band close to the Fermi level upon only a slight delithiation yielding $Li_{0.99}CoO_2$ (dashed red curve). Such abrupt shift of the Co-t_{2g} band to the Fermi level could already lead to a significant increase in absorbance or conductivity. Obviously, the present understanding of the electronic structure is in good agreement with our observations.

Figure 6b shows the evolution of the real part of the CRI of LCO upon de/lithiation. In the region of resonance or strong electronic transition ($400\text{ nm} < \lambda < 700\text{ nm}$), there is a region of anomalous dispersion i.e. the real part falls below 1. In general, beyond this resonance, for wavelengths longer than 700 nm, the removal of lithium increases the real part of the CRI.

Furthermore, using Eq. 5, the overall higher value of the reflectance spectrum in the ex situ case when compared to the in-operando case also becomes evidently clear. The larger the difference in the refractive indices is, the larger is the reflection coefficient. From literature, the real part of the refractive index of dimethyl carbonate is 1.36[52] and that of ethylene carbonate is 1.416.[53] Therefore, the electrolyte consisting of these two components is expected to certainly exhibit a refractive index of more than 1 (for air). Therefore, the reflection coefficient for the LCO/air interface is higher than that for LCO/electrolyte interface and hence, the net reflection is also higher in the former case.

As mentioned in the introduction, an optical switching device could be a potential application of the electrochromic effect. However, some important material parameters are important for such application, namely phase modulation and insertion loss along with the extinction ratio (ER).

These parameters are determined by the change in the real part and imaginary part of the CRI upon lithium removal, as shown in Fig. 7. The phase modulation, $\Delta\varphi$, caused by a change in the real part of the CRI upon lithium insertion (Δn), for an optical path length L is given by:

$$\Delta\varphi = \frac{2\pi}{\lambda}\cdot\Delta n\cdot L \qquad [7]$$

However, simultaneously there would be insertion losses (IL), which are defined by:

$$\mathrm{IL} = -10\cdot\log_{10}[e^{\left(\frac{-4\pi k}{\lambda}\cdot L\right)}], \qquad [8]$$

where k is the imaginary part of the CRI. These insertion losses would also change by the insertion/removal of lithium, defined by the extinction ratio (ER) as:

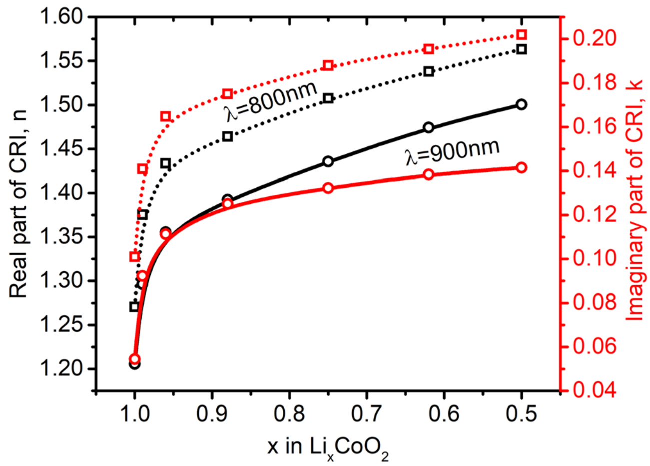

Figure 7. Change of real (black lines) and imaginary (red lines) part of complex refractive index (CRI) for different charge states for LCO at 800 nm (dotted line, and square symbols) and 900 nm (solid line and circular symbols) wavelengths.

$$ER = IL_{x=1 \text{ in } Li_xCoO_2} - IL_{x=0.5 \text{ in } Li_xCoO_2}, \quad [9]$$

Using Eq. 7 and data from Fig. 7, a phase shift of π can be enabled by using 1.367 μm (with 800 nm wavelength) and 1.526 μm (with 900 nm wavelength) of LCO (by changing x in Li_xCoO_2 from 1 to 0.5). However, the former (λ = 800 nm) would cause a change of 9.2 dB in the ER (I/I_0 changing from 11% to 1.3%); the latter (λ = 900 nm) yields an ER = 8.05 dB (I/I_0 changing from 30% to 5%).

However, if the device would be used as an absorber of light i.e., switching the intensity, then an ER value of 30 dB is achieved by a length of 5.7 μm of LCO with λ = 900 nm (by varying the x in Li_xCoO_2 from 1 to 0.5).

Phase propagation.—Once the optical properties have been quantified at different charge states, for a material exhibiting a phase transformation, they can be used to examine the geometrical distribution of phases.[12] Firstly, we determine the dielectric constants from the optical constants using:

$$\hat{n}^2 = \varepsilon = n^2 - k^2 - i{\cdot}2nk = \varepsilon_{Re} - i\varepsilon_{im}$$

$$\varepsilon_{Re} = n^2 - k^2;\ \varepsilon_{im} = 2nk \quad [10]$$

where ε_{Re} and ε_{im} are the real and imaginary part of the complex dielectric function; n and k are the real and imaginary part of CRI. For a heterogeneous distribution of phases in a two-phase material, the effective dielectric constant is dependent on the geometrical arrangement of phases and their individual dielectric constants.[29,30] If the Li_1CoO_2 and $Li_{0.5}CoO_2$ phases are stacked on top of each other and light is incident perpendicular to this stack (i.e., the electro-magnetic field is parallel to the planar distribution of phases, see Fig. 8 top-left inset) the effective dielectric function is given by Eq. 11 (serial summation).

$$\varepsilon = f_{LiCoO_2}\varepsilon_{LiCoO_2} + f_{Li_{0.5}CoO_2}\varepsilon_{Li_{0.5}CoO_2} \quad [11]$$

where f_i and ε_i are the volume fraction and dielectric constant of the i th phase. However, when the phases are stacked side by side (similar to the columnar distribution of phases), see bottom-right inset in Fig. 8, and the path of propagation of light is oriented parallel to the stack, the effective dielectric function is given by Eq. 12 (parallel summation).

$$\frac{1}{\varepsilon} = \frac{1}{f_{LiCoO_2}\varepsilon_{LiCoO_2}} + \frac{1}{f_{Li_{0.5}CoO_2}\varepsilon_{Li_{0.5}CoO_2}} \quad [12]$$

If the imaginary part of the complex dielectric function is plotted versus the real part, it will be a straight line for planar stacking (red dashed line in Fig. 8), while a hyperbolic section is obtained for stacking side by side (blue dotted line). The observed dielectric constants at different charge states are shown by black points in Fig. 8. These values are calculated by Eq. 10 (with the values of n and k from Figs. 6a and 6b) for a particular wavelength of 850 nm which is away from the anomalous dispersion region. These data points match more closely to the straight red dashed line, in fact even slightly deviating upwards, but certainly do not match the inversely curved behavior of the blue-dotted line. This indicates a layered arrangement of the two hexagonal phases, which are distinguishable by the differences in their optical properties. When this behavior is compared to a different battery material, namely $Li_4Ti_5O_{12}$ (LTO) see Fig. 8c,[12] a remarkable difference becomes obvious. In the case of LTO, it was indicated that grain boundaries provide the nucleation sites of the Li-rich phase and due to the columnar distribution of grains, the behavior was better described by a side by side stacking model. This is in contrast to the current case, although also here the grain boundaries seem to be predominantly perpendicular to the substrate (see dark-field TEM image, Fig. 2c). Very likely the grain boundaries are not providing a significantly faster path for diffusion in $LiCoO_2$. This can be understood if we look closely at the structure of the LCO and the orientation of the grain boundaries (black arrow) as shown in Fig. 8b (structure taken from[54]). From the figure, it can be seen that the interplanar spacing between the CoO_6 octahedra corresponds to roughly 0.26 nm. This is larger than the diameter of the lithium atom which is probably between 0.25 nm to 0.18 nm (covalent radius of 0.128 nm[55] and ionic radius of 0.09 nm[56]). Obviously, the values of these radii are only approximate and it will depend on the type of bonding, nevertheless, it enables us to understand why lithium can be easily and reversibly de/intercalated in between the layers of CoO_6 octahedra in LCO. Therefore, in between these CoO_6 octahedra, the diffusion of lithium could be comparable to the grain boundary diffusion. So far there are no experimental values of grain boundary diffusion of lithium in this material. However, Xia and Lu[38] prepared (003) and (104) textured thin films and measured the average diffusion in both. They found that in the (003)- textured sample the electrochemical performance was almost comparable. This comparable performance was ascribed to the grain boundary diffusion in the case of (003)-textured films. The slightly lowered average diffusion coefficient in (003)- textured sample, reported by them, is probably due to the fact, that in this particular texture the CoO_6 octahedral planes (003) blocking the perpendicular migration of lithium, and if the grain boundary density is not high enough then it would yield a lowered average diffusion coefficient.

Now, in the present case, due to the (101)-texture and a huge c/a ratio (ca. 5[34]) in LCO, the basal planes or CoO_6 octahedral planes are almost parallel to the direction of lithium insertion i.e. they stand almost perpendicular to the surface of the film (a 10° inclination, as can be seen in Fig. 8b). Meaning the migration of lithium (in between the CoO_6 octahedra) for this particular (101)- texture may be comparable (if not faster) to the grain boundary diffusion. This would result in a layered-like phase propagation as is evidenced by the optical measurements. Therefore, in this studied case a Harrison type A kinetics[57] is observed from the very beginning. It would be interesting to see a similar study, but with a (003)-textured film, where it has been claimed that grain boundaries contribute significantly to the migration of lithium, however, this is beyond the scope of the current paper focusing on the optical properties.

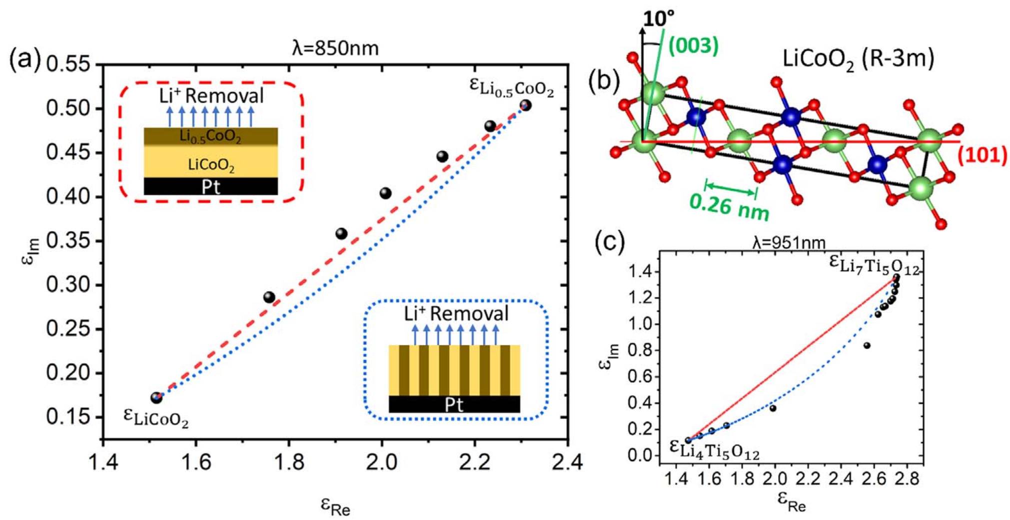

Figure 8. (a) Real and imaginary part of dielectric constants for different charge states for LCO; (b) The inclination of the (003)- planes, or plane of fastest migration, due to a texture along (101)- direction. The black arrow marks the growth direction or the ideal alignment of grain boundaries in a columnar microstructure. The red line is in the (101)- plane and hence parallel to the substrate. The structure is taken from Ref. 54: red, blue, and green atoms are oxygen, cobalt, and lithium; (c) the real vs the imaginary part evolution upon lithiation in $Li_{4+x}Ti_5O_{12}$.[12]

Conclusion

The optical response of sputter-deposited thin films of LCO has been investigated during the Li intercalation using in-operando and ex situ reflectance spectroscopy. The sputter deposition process and subsequent annealing result in a preferential orientation of the grains with the (101)- axis in the growth direction. The films were electrochemically characterized to show a reversible de/intercalation of lithium. Subsequently, using in-operando reflectance spectroscopy a reversible optical response upon Li insertion/removal was observed. To quantify the evolution of the optical spectrum during changing Li content, well-defined intercalation states were prepared and measured using ex situ optical spectroscopy. The obtained reflectance spectra were modeled by applying the Clausius-Mossotti relation. From the model description, the real and imaginary parts of the complex refractive index (CRI) at different charged states were obtained. The measurement revealed a band-gap of 1.9 eV for the completely lithiated LCO (or hexagonal type I phase). The band-gap was obtained by correlating a dominant peak in the imaginary part of CRI to the electronic transition from the Co-t_{2g} to the Co-$e_{.g.}$ band. Upon Li deintercalation, this electronic transition energy was observed to increase which was rationalized by a widening of the energy gap between these bands, as was reported by a previous study. Furthermore, the enhanced conductivity of the hexagonal type II phase is observed as a much broader and larger imaginary part of the CRI when compared to the completely lithiated LCO. Finally, from the CRI, the complex dielectric constants were determined. The variation of the real part and the imaginary part of dielectric constants upon changing Li content strongly indicates a layered like phase propagation during de/lithiation. This is probably due to comparable Li migration rates in the volume of the grains and the grain boundaries in the (101)-textured thin films.

Acknowledgments

We are grateful to the continuous infrastructural support by the University of Stuttgart. Sadly, the German Science foundation refused several times funding of this and our other works on optical properties and light switching with battery materials.[11,12,28]

ORCID

Yug Joshi https://orcid.org/0000-0001-7920-5890

References

1. M. V. Reddy, A. Mauger, C. M. Julien, A. Paolella, and K. Zaghib, *Materials (Basel).*, **13**, 1884 (2020).
2. W. D. Johnston, R. R. Heikes, and D. Sestrich, *J. Phys. Chem. Solids*, **7**, 1 (1958).
3. H. J. Orman and P. J. Wiseman, *Acta Cryst. C*, **40**, 12 (1984).
4. K. Mizushima, P. C. Jones, P. J. Wiseman, and J. B. Goodenough, *Mat. Res. Bull*, **15**, 789 (1980).
5. T. Ohzuku and A. Ueda, *J. Electrochem. Soc.*, **141**, 2972 (1994).
6. Q. Zhang and R. E. White, *J. Electrochem. Soc.*, **154**, A587 (2007).
7. A. Van der Ven, M. K. Aydinol, G. Ceder, G. Kresse, and J. Hafner, *Phys. Rev. B*, **58**, 2975 (1998).
8. K. Mukai, H. Nozaki, Y. Ikedo, J. Sugiyama, K. Ariyoshi, and T. Ohzuku, *J. Power Sources*, **192**, 684 (2009).
9. S. Laubach, S. Laubach, P. C. Schmidt, D. Ensling, S. Schmid, W. Jaegermann, A. Thißen, K. Nikolowski, and H. Ehrenberg, *Phys. Chem. Chem. Phys.*, **11**, 3278 (2009).
10. H. Kang, J. Lee, T. Rodgers, J.-H. Shim, and S. Lee, *J. Phys. Chem. C*, **123**, 17703 (2019).
11. Y. Joshi, R. Lawitzki, and G. Schmitz, *Small Methods*, **5**, 2100532 (2021).
12. Y. Joshi, A. Saksena, E. Hadjixenophontos, J. M. Schneider, and G. Schmitz, *ACS Appl. Mater. Interfaces*, **12**, 10616 (2020).
13. A. J. Merryweather, C. Schnedermann, Q. Jacquet, C. P. Grey, and A. Rao, *Nat.*, **594**, 522 (2021).
14. F. Rittweger, C. Modrzynski, V. Roscher, D. L. Danilov, P. H. L. Notten, and K.-R. Riemschneider, *J. Power Sources*, **482**, 228943 (2021).
15. F. Berkemeier, T. Stockhoff, T. Gallasch, and G. Schmitz, *Acta Mater.*, **80**, 132 (2014).
16. M. Muñoz-Castro, N. Walter, J. K. Prü, W. Pernice, and H. Bracht, *ACS Photonics*, **6**, 1182 (2019).
17. C. G. Granqvist, *Handbook of Inorganic Electrochromic Materials* (Elsevier, Amsterdam) pp.1 (1995).
18. J. S. E. M. Svensson and C. G. Granqvist, *Sol. Energy Mater.*, **11**, 29 (1984).
19. S. Zeb, G. Sun, Y. Nie, H. Xu, Y. Cui, and X. Jiang, *Mater. Adv.*, **2**, 6839 (2021).
20. T. G. Manivasagam, K. Kiraz, and P. H. L. Notten, *Crystals*, **2**, 1410 (2012).
21. S. Bao, K. Tajima, Y. Yamada, M. Okada, and K. Yoshimura, *Sol. Energy Mater. Sol. Cells*, **92**, 224 (2008).
22. F. Michalak, K. von Rottkay, T. Richardson, J. Slack, and M. Rubin, *Electrochim. Acta*, **44**, 3085 (1999).
23. P. H. L. Molten, M. Kremers, and R. Griessen, *J. Electrochem. Soc.*, **143**, 3348 (1996).
24. M. Muñoz-Castro, F. Berkemeier, G. Schmitz, A. Buchheit, and H.-D. Wiemhöfer, *J. Appl. Phys.*, **120**, 135106 (2016).
25. Y. Zhai, J. Li, S. Shen, Z. Zhu, S. Mao, X. Xiao, C. Zhu, J. Tang, X. Lu, and J. Chen, *Adv. Funct. Mater.*, 2109848 (2022).
26. R. Clausius, *Die Mechanische Behandlung der Electricität* (Vieweg Teubner Verlag, Wiesbaden) pp.352 (1879).
27. O. Mossotti, *Discussione analitica sull'influenza che l'azione di un mezzo dielettrico ha sulla distribuzione dell'elettricità alla superficie di più corpi elettrici disseminati* (Dai tipi della r. D. camera, Modena, Italy) (1846).
28. Y. Joshi, E. Hadjixenophontos, S. Nowak, R. Lawitzki, P. K. Ghosh, and G. Schmitz, *Adv. Opt. Mater.*, **6**, 1701362 (2018).
29. E. E. Chain and D. M. Byrne, *Thin Solid Films*, **181**, 323 (1989).

30. O. Stenzel, *The Physics of Thin Film Optical Spectra: An Introduction* (Springer, Cham, Switzerland) 2nd ed. ed., Chapter 1 (2015).
31. H. A. Müller, Y. Joshi, E. Hadjixenophontos, C. Peter, G. Csiszár, G. Richter, and G. Schmitz, *RSC Adv.*, **10**, 3636 (2020).
32. J. Mürter, S. Nowak, E. Hadjixenophontos, Y. Joshi, and G. Schmitz, *Nano Energy*, **43**, 340 (2017).
33. S. Nowak, F. Berkemeier, and G. Schmitz, *J. Power Sources*, **275**, 144 (2015).
34. T. Stockhoff, T. Gallasch, F. Berkemeier, and G. Schmitz, *Thin Solid Films*, **520**, 3668 (2012).
35. E. Antolini and M. Ferretti, *J. Solid State Chem.*, **117**, 1 (1995).
36. L. A. Giannuzzi, B. W. Kempshall, S. M. Schwarz, J. K. Lomness, B. I. Prenitzer, and F. A. Stevie, “FIB Lift-Out Specimen Preparation Techniques.” *Introduction to Focused Ion Beams: Instrumentation, Theory, Techniques and Practice* (Springer, Boston, Massachusetts) 1, 201 (2005).
37. J. M. Rosolen, P. Ballirano, M. Berrettoni, F. Decker, and M. Gregorkiewitz, *Ionics*, **3**, 345 (1997).
38. H. Xia and L. Lu, *Electrochim. Acta*, **52**, 7014 (2007).
39. J. Hong and J. R. Selman, *J. Electrochem. Soc.*, **147**, 3183 (2000).
40. J. N. Reimers and J. R. Dahn, *J. Electrochem. Soc.*, **139**, 2091 (1992).
41. Y. Gu, D. Chen, and X. Jiao, *J. Phys. Chem. B*, **109**, 17901 (2005).
42. M. Ménétrier, I. Saadoune, S. Levasseur, and C. Delmas, *J. Mater. Chem.*, **9**, 1135 (1999).
43. E. Hecht, *Optics* (Addison-Wesley, Reading, Massachusetts) (2002).
44. Beer, *Ann. der Phys.*, **162**, 78 (1852).
45. J. H. Lambert, *Photometrie: Photometria sive de mensura et gradibus luminis, colorum et umbrae* (Verlag von Wilhelm Engelmann, Leipzig) (1760).
46. O. S. Heavens, *Rep. Prog. Phys.*, **23**, 1 (1960).
47. W. S. M. M. Werner, K. Glantschnig, and C. Ambrosch-Draxl, *J. Phys. Chem. Ref. Data*, **38**, 1013 (2009).
48. A. Milewska, K. Świerczek, J. Tobola, F. Boudoire, Y. Hu, D. K. Bora, B. S. Mun, A. Braun, and J. Molenda, *Solid State Ionics*, **263**, 110 (2014).
49. P. Ghosh, S. Mahanty, M. W. Raja, R. N. Basu, and H. S. Maiti, *J. Mater. Res.*, **22**, 1162 (2007).
50. J. M. Rosolen and F. Decker, *J. Electroanal. Chem.*, **501**, 253 (2001).
51. J. Van Elp, J. L. Wieland, H. Eskes, P. Kuiper, G. A. Sawatzky, F. M. F. De Groot, and T. S. Turner, *Phys. Rev. B*, **44**, 6090 (1991).
52. A. Rodríguez, J. Canosa, and J. Tojo, *J. Chem. Eng. Data*, **46**, 1476 (2001).
53. A. Wypych and G. Wypych, *Databook of Green Solvents* (ChemTec Publishing, Toronto, Ontario) pp.237 (2014).
54. Y. Takahashi, N. Kijima, K. Dokko, M. Nishizawa, I. Uchida, and J. Akimoto, *J. Solid State Chem.*, **180**, 313 (2007).
55. B. Cordero, V. Gómez, A. E. Platero-Prats, M. Revés, J. Echeverría, E. Cremades, F. Barragán, and S. Alvarez, *Dalt. Trans.*, 2832 (2008).
56. R. D. Shannon, *Acta Crystallogr., Sect. A*, **32**, 751 (1976).
57. L. G. Harrison, *Trans. Faraday Soc.*, **57**, 1191 (1961).